Delaying precipitation by air pollution over the Pearl River Delta: 2. Model simulations

Seoung Soo Lee[1], Jianping Guo[2], and Zhanqing Li[1,3]

[1]Department of Atmospheric and Oceanic Sciences and Earth System Science Interdisciplinary Center, University of Maryland, College Park, Maryland, USA, [2]State Key Laboratory of Severe Weather and Key Laboratory of Atmospheric Chemistry of CMA, Chinese Academy of Meteorological Sciences, Beijing, China, [3]College of Global Change and Earth System Science, and State Key Laboratory of Earth Surface Processes and Resource Ecology, Beijing Normal University, Beijing, China

Abstract In Part 1 of two companion studies, analyses of observational data over the Pearl River Delta of China showed that larger aerosol concentrations (polluted conditions) resulted in suppressed precipitation before the midafternoon while resulting in enhanced precipitation after the midafternoon when compared to precipitation with smaller aerosol concentrations (clean conditions). This suggests that there is a tipping point in the transition from suppressing to enhancing precipitation with increases in aerosol concentration. This paper aims to identify mechanisms that control the tipping point by performing simulations. Simulations show that during the first three quarters of the 12 h simulation period, aerosol as a radiation absorber suppresses convection and precipitation by inducing greater radiative heating and stability. Convection weakens and precipitation reduces more under polluted conditions than under clean conditions. Due to the suppressed convection, the depletion of convective energy decreases. The reduced depletion of convective energy during the period of the suppressed convection boosts the level of stored energy after this period. The boosted level of stored energy enables updrafts to be strong enough to transport a greater amount of cloud liquid to the freezing level and to levels above it under polluted conditions than under clean conditions. This in turn induces greater freezing-related latent heating, buoyancy, and thus stronger convection and results in the transition from lower precipitation rates during the first three quarters of the simulation period to higher precipitation rates during the last quarter of the period under polluted conditions than under clean conditions.

1. Introduction

Aerosols, which are able to scatter and absorb solar radiation, can alter atmospheric stability by changing both surface heat fluxes and radiative heating of the atmosphere [*Segal et al.*, 1989; *Hansen et al.*, 1997; *Li*, 1998; *Feingold et al.*, 2005; *Jacobson*, 2006, 2012; *Davidi et al.*, 2009; *Li et al.*, 2010]. This effect of aerosols is referred to as aerosol radiative effects in this study. For example, aerosols that act as radiation absorbers enhance the radiative heating of the atmosphere by intercepting incident solar radiation. This interception diminishes the amount of solar radiation that reaches the surface and thus tends to lower surface heat fluxes. Studies [e.g., *Ackerman et al.*, 2000; *Koren et al.*, 2004; *Hill and Dobbie*, 2008; *Koch and Del Genio*, 2010] have shown that aerosol-induced reduction in surface heat fluxes and enhancement of the radiative heating of the atmosphere suppress convection and clouds.

Aerosols also affect clouds by acting as cloud condensation nuclei (CCN) and ice nuclei (IN) [*Feingold et al.*, 2005; *van den Heever et al.*, 2006; *Grabowski*, 2006; *Khain and Lynn*, 2009; *Morrison and Grabowski*, 2011; *van den Heever et al.*, 2011; *Guo et al.*, 2014]. This effect is referred to as the aerosol microphysical effects in this study. When aerosols act as CCN, the increase in the aerosol number concentration reduces autoconversion. Here autoconversion is defined to be the process that converts cloud droplets to raindrops through collision and collection between cloud droplets [*Kessler*, 1969]. The reduction in autoconversion means that there is a smaller amount of cloud droplets or cloud liquid that is converted to rain. Hence, the reduction in autoconversion raises the ratio of cloud-liquid mass to rain mass for a given total amount of cloud water. Most of this escalation in the ratio occurs below the level of freezing in mixed-phase convective clouds [*Khain et al.*, 2005; *Seifert and Beheng*, 2006; *Tao et al.*, 2007, 2012; *van den Heever and Cotton*, 2007; *Lee et al.*, 2010; *Storer et al.*, 2010; *Lee*, 2011]. The enhanced ratio of cloud-liquid (or droplet) mass enables the mass of cloud liquid that is transported to altitudes above the freezing level to be greater, which in turn results in a larger amount of frozen cloud liquid for a given total amount of cloud water in convective clouds. This boosts the latent heat release, which enables air parcels to have greater thermal buoyancy and thus

more intense updrafts. These intensified updrafts are a good indication of the invigoration of convection, which produces more cloud water and precipitation [*Rosenfeld et al.*, 2008; *Li et al.*, 2011; *Tao et al.*, 2012].

Aerosol radiative effects which are associated with aerosol-induced suppression of convection compete with aerosol microphysical effects which are associated with aerosol-induced invigoration of convection as found by *Koren et al.* [2008] and *Ten Hoeve et al.* [2012]. In cases where aerosol radiative effects are dominant over aerosol microphysical effects, suppression of convection and precipitation are observed, while in other cases where aerosol microphysical effects are dominant over aerosol radiative effects, invigoration of convection and enhanced precipitation are observed [*Koren et al.*, 2008; *Ten Hoeve et al.*, 2012].

The competition between aerosol radiative effects and aerosol microphysical effects is inferred to explain the occurrence of the tipping point found in observations in our companion paper [*Guo et al.*, 2016, hereafter Part 1]. Based on extensive analyses of data collected in the Pearl River Delta (PRD) region in south China where pollution is typically heavy [*Guo et al.*, 2011], diurnal variations in precipitation associated with thunderstorms were found to be correlated with aerosol loading as represented by the mass of aerosol particles up to 10 μm in diameter (PM$_{10}$). A tipping point was found where a switch in the response of precipitation to increases in pollution level occurred. Before the midafternoon, there was a larger amount of precipitation under low aerosol loading conditions (PM$_{10}$ below 42 μg m^{-3}, clean conditions) than under high aerosol loading conditions (PM$_{10}$ above 57 μg m^{-3}, polluted conditions). However, after this time, the situation was reversed; i.e., there was a larger amount of precipitation under polluted conditions than under clean conditions. The tipping point was hypothesized to be dictated by two primary mechanisms: aerosol radiative effects and aerosol microphysical effects.

While *Koren et al.* [2008] and *Ten Hoeve et al.* [2012] have provided some valuable insights into the competition between the two types of aerosol effects, they did not examine the diurnal variation in the competition and its impacts on the diurnal variation in clouds and precipitation, since clouds and precipitation in those studies were averaged over the diurnal cycle. As a result, our level of understanding of the mechanisms that control the effects of the diurnal variation in the competition on the diurnal variation in clouds and precipitation is low. This indicates that we need to perform further studies to understand the mechanisms that control the tipping point.

To this end, numerical simulations are performed using a cloud-system resolving model (CSRM), which resolves cloud-scale microphysics, dynamics, and their feedbacks, thus enabling us to gain deep insights into the mechanisms that are associated with cloud-scale processes. The simulations are for a mesoscale cloud ensemble (MCE), which involves deep convective mixed-phase clouds. These clouds are the dominant cloud type studied in Part 1.

The CSRM employed in this study is introduced in section 2, followed by a description of the simulated cases and simulations in section 3. Section 4 presents and analyzes the results of the simulations with reference to observed phenomena. Summary and conclusions are given in section 5.

2. The CSRM

The Advanced Research Weather Research and Forecasting (ARW) model (version 3.3.1), a three-dimensional nonhydrostatic compressible model, is used here as the CSRM. A detailed description of the governing equations, numerical methods, and physics of the ARW model is documented by *Skamarock et al.* [2008]. Shortwave and longwave radiation parameterizations have been included in all simulations by adopting the Rapid Radiation Transfer Model [*Fouquart and Bonnel*, 1980; *Mlawer et al.*, 1997]. Microphysical processes are represented by a double-moment bin-bulk scheme that uses bin-model-derived look-up tables for hydrometeor collection processes [*Saleeby and Cotton*, 2004; *Lee et al.*, 2010]. A gamma size distribution with fixed breadth is assumed for hydrometeor size distributions. Cloud-droplet and ice-crystal nucleation mimic a size-resolved approach [*Lee and Feingold*, 2010; *Lee*, 2012]. More details of the double-moment scheme used in this study are found in *Saleeby and Cotton* [2004] and *Lee et al.* [2010].

Using the Noah land surface model (LSM) [*Chen and Dudhia*, 2001], surface heat fluxes are predicted. For the land surface, the LSM has one canopy layer and the following variables are predicted in the LSM: soil moisture and temperature in the soil layers, water stored on the canopy, and snow stored on the ground. The multilayer soil model developed by *Pan and Mahrt* [1987] is coupled to the LSM to capture the evolution
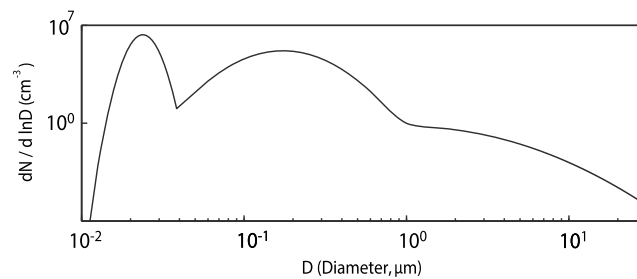
Figure 1. Aerosol size distribution at the surface. *N* represents the aerosol number concentration per unit volume of air, and *D* represents the aerosol diameter.

of soil moisture and temperature by considering incident solar and long-wave radiation onto the surface which serves as the primary heat source for soil layers and heat and moisture distribution processes in those layers. The LSM uses four soil layers.

Aerosols are assumed to be internal mixtures of black carbon (BC, 9% mass) and sulfate (91% mass) [*Zhang et al.*, 2012]. The radiative effect of aerosols is included in the simulations and is represented by a method similar to that described by *Feingold et al.* [2005]. The internal aerosol mixture and the ARW-predicted relative humidity are used to calculate the hygroscopic growth of the aerosol particles and their optical properties, i.e., extinction, the single scattering albedo (SSA), and the phase function. A volume mixing rule is used to calculate the refractive index of the hydrated particles. The SSA of aerosol particles is 0.88 at 470 nm in this study. This SSA value corresponds to the mean SSA in the PRD region over the summer seasons of 2008–2012 which is the target region and period in Part 1.

Prognostic equations are solved for the aerosol mass mixing ratio. The aerosol mass mixing ratio is advected, diffused, and depleted by activation and washout by precipitable hydrometeors (i.e., nucleation and impacting scavenging) during the simulation. The prognosed supersaturation of air parcels is used to explicitly activate aerosol particles. After activation, the aerosol mass is transported within hydrometeors by collision-coalescence and removed from the atmosphere once hydrometeors that contain aerosols reach the surface. Following *Feingold and Kreidenweis* [2002], we assume that when a portion of the total hydrometeor mass of an original (hydrometeor) class is transported to a different class by microphysical processes such as collision-coalescence, the ratio of the aerosol mass (to the total aerosol mass) that is transported from the original class (in which the total aerosol mass is embedded before the transportation) to the different class is the same as the ratio of the hydrometeor mass (to the total hydrometeor mass before the transportation) of the original class that is transported. Aerosols return to the atmosphere upon evaporation or sublimation of hydrometeors that contain aerosols.

The size distribution is assumed to be trimodal lognormal and invariant, based on observations made at Guangzhou in the PRD region [*Peng et al.*, 2014]. The modal diameter and distribution breadth of each of the modes of the size distribution are assumed to be homogenous in time and space, so aerosol particles at any grid point in simulations in this study have the shape of the size distribution shown in Figure 1. Figure 1 shows the initial size distribution of background aerosol particles at the surface. This means that advected and diffused aerosols and aerosols included in cloud particles via scavenging and returned to the atmosphere via evaporation and sublimation of cloud particles take on the shape of the size distribution shown in Figure 1. Based on the assumed trimodal lognormal distribution, the predicted aerosol mass is used to diagnose the aerosol number concentration that varies spatiotemporally due to clouds, advection, and diffusion.

3. Case Description and Numerical Simulations

The selected study area in the PRD region for Part 1, as marked by the red rectangle in Figure 2, is a polluted mesoscale domain that has a length of ~100 km in both directions. Since this study focuses on mechanisms that control the tipping point observed in this study area, the size of the simulation domain for this study should be comparable to that of the study area. Hence, three-dimensional simulations of an observed mesoscale system or MCE of mixed-phase convective clouds in the study area are made over a domain whose length is 120 km in both horizontal directions and 20 km in the vertical direction. The horizontal (vertical) grid length is 1 km (200 m). The domain size adopted here is able to capture the mesoscale structure of the system. The resolution adopted here is known to resolve convective or updraft cores reasonably well [*Tao*, 2007; *Lee et al.*, 2008a].

The system was observed from 06:00 Beijing time (BJT, close to the local solar time) to 18:00 BJT, on 17 June 2013 over Guangzhou (23.13°N, 113.27°E) in the PRD region. Figure 3 depicts the spatial distribution of cloud
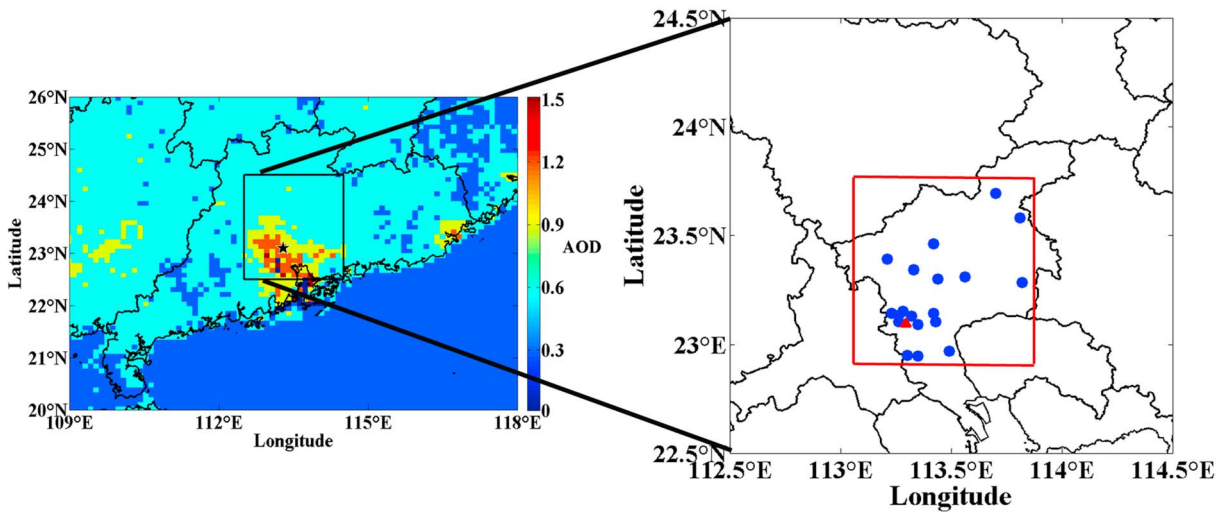
Figure 2. Location of the study area. (left) The spatial distribution of the mean summertime (June through August) Moderate Resolution Imaging Spectroradiometer aerosol optical depth averaged over 2008–2012. (right) Locations of the 19 air quality observation stations (blue dots). The red triangle in Figure 2 (right) shows the location of Guangzhou (23.1°N, 113.3°E). The spatial extent of the 19 locations determines the selected study area that is marked by the red rectangle (22.9°N–23.7°N, 113.2°E–113.8°E). Adapted from Part 1 [*Guo et al.*, 2016].

reflectivity observed by the Geostationary Operational Environmental Satellite at 15:00 BJT around the mature stage of the system in the selected study area. Cloud cells are not organized in any particular way over the horizontal domain unlike if squall lines, for example, were present (Figure 3). This supports the use of periodic boundary conditions that are applied on the horizontal boundaries. This system is characterized by weak convection in the morning and strong convection in the afternoon.

Soundings from radiosondes launched every 6 h during the period when the cloud system was observed were collected. Measurements were taken at a 1 s resolution with measurement oscillations and noise removed during the ascent of the radiosondes. We calculate tendencies (or rates of temporal changes) of potential temperature and specific humidity based on the 6-hourly soundings. These tendencies represent the advection of temperature and humidity into or out of the model domain by large- or synoptic-scale motions based on the assumption that the soundings represent large- or synoptic-scale environments. Hence, these tendencies can represent the convergence of temperature and humidity into the model domain or the divergence of temperature and humidity out of the model domain by large- or synoptic-scale motions. These tendencies are referred to as large-scale forcings. Large-scale forcings are considered in simulations by adding the tendencies to prediction equations for potential temperature and specific humidity. Large-scale forcings are applied to the model every time step by temporal interpolation, a technique that has been frequently used in CSRM comparison studies [e.g., *Xu et al.*, 2002; *van Zanten et al.*, 2011; *Varble*
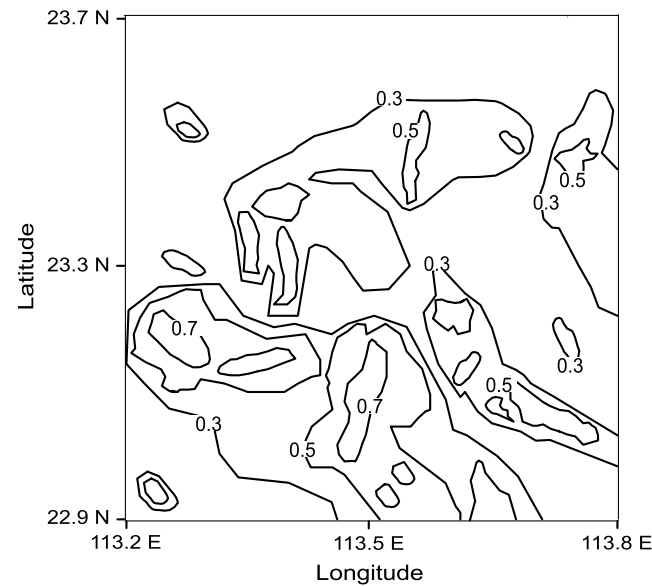

Figure 3. Cloud-reflectivity field observed by the Geostationary Operational Environmental Satellite at 15:00 BJT on 17 June 2013. This is around the mature stage of the cloud system in the selected study area that is marked by the red rectangle in Figure 2.

et al., 2011; *Fridlind et al.*, 2012]. Details of the procedure for applying large-scale forcings are described by *Fridlind et al.* [2010]. The horizontal momentum is damped to observed values following *Xu et al.* [2002].

For all simulations in this study, identical large-scale forcings are applied. Hence, the identical advection, convergence, and divergence of temperature and humidity at synoptic scales are applied to all simulations in this study. However, large-scale forcings do not entirely dictate cloud processes at cloud or convection scales. Thus, despite the identical large-scale forcings, simulations with different setups of aerosol properties (of interest to us for this study) will result in different cloud processes.

The use of periodic boundary conditions ensures that the total water and heat energy supplied to and removed from the domain by large-scale forcings are identical between simulations. This enables the isolation of the effect of aerosols on interactions between microphysics and dynamics at cloud scales in this study.

Random perturbations of the potential temperature are imposed on simulations at the first time step as a way of initiating or triggering convection. The perturbations vary in the horizontal but are constant throughout the lowest 1.5 km in each column of the model. The perturbations are horizontally random, generated from a uniform distribution between −0.1 and +0.1 K. These perturbations are similar to those employed by *Donner et al.* [1999] and *Lee et al.* [2014] and are chosen to be random so as not to impose organized structure on convection when it develops.

In the planetary boundary layer (PBL), the background aerosol number concentration integrated over the distribution at the beginning of the simulation period at Guangzhou is 7500 cm^{-3}. In the PBL, the aerosol concentration is constant; however, beyond the PBL, it decreases exponentially with altitude. The first simulation is performed with this aerosol concentration of 7500 cm^{-3} as an initial background aerosol concentration in the PBL and is referred to as the "control run." To examine the effect of aerosols on the precipitating cloud system, the control run is repeated with the aerosol number concentration decreased by a factor of 10. This simulation is referred to as the "low-aerosol run." Note that both aerosol radiative and microphysical effects are included in the control run and the low-aerosol run. To examine aerosol radiative effects on cloud development as compared to aerosol microphysical effects, the control run and low-aerosol run are repeated with no consideration of the effect of aerosols on radiation, i.e., before the activation of aerosol particles into droplets. These repeated runs are referred to as the "control-no-rad run" and the "low-aerosol-no-rad run," respectively. Hence, in the control-no-rad run and the low-aerosol-no-rad run, only aerosol microphysical effects are present.

In this study, on average, around 30% of aerosol particles are activated in updrafts. The mean cloud droplet number concentration (CDNC) over grid points with nonzero CDNC in the PBL is 2300 and 2400 cm^{-3} in the control run and the control-no-rad run, respectively, and 220 and 270 cm^{-3} in the low-aerosol run and low-aerosol-no-rad run, respectively.

4. Results

4.1. Overall Evolution of Precipitation

Figure 4a shows the time series of the simulated domain-averaged precipitation rates for the four runs. Comparisons between observed and simulated precipitation in the control run indicate that the evolution of the simulated precipitation follows its observed counterpart reasonably well. The observed precipitation rates are averaged over all rain gauges every 3 h over the 12 h simulation period on 17 June 2013 in the selected study area for which the simulation domain is defined. The standard deviation of observed precipitation rates at each of the observation times ranges between 0.1 and 0.3 mm h^{-1}. The domain-averaged cumulative precipitation at the last time step is 14.5, 11.6, 15.8, and 14.3 mm in the control run, the low-aerosol run, the control-no-rad run, and the low-aerosol-no-rad run, respectively.

When the effect of aerosols on radiation is not considered, the precipitation rate of the control-no-rad run is greater than that of the low-aerosol-no-rad run during the simulation period. This is induced by aerosol-induced greater freezing of cloud liquid and the invigoration of convection as shown by *Rosenfeld et al.* [2008] (see sections 4.2 and 4.8 for analyses of freezing and additional simulations that support this invigoration). Figures 4b and 4c show the time series of the domain-averaged precipitation rates that are produced by cold and warm clouds, respectively. In this study, clouds are classified into warm clouds (with tops below the freezing level) and cold clouds (with tops at and above the freezing level). Note that the simulated time- and
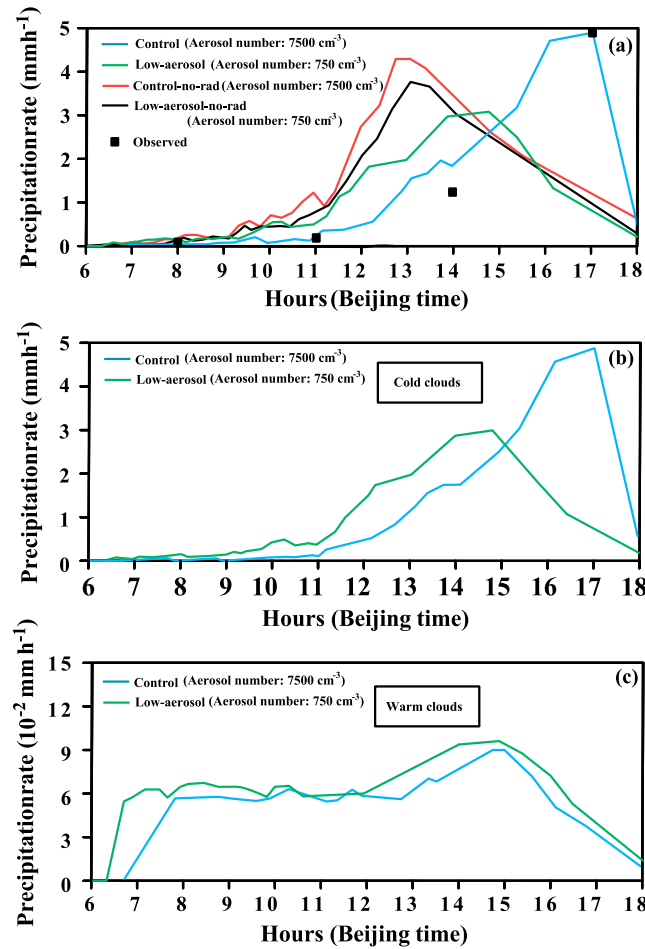
Figure 4. Time series of the domain-averaged precipitation rates from the ARW model simulations (a) under clean conditions (the low-aerosol run and the low-aerosol-no-rad run, represented by green and black lines, respectively) and polluted conditions (the control run and the control-no-rad run, represented by blue and red lines, respectively), and for precipitation that is produced by (b) cold clouds and (c) warm clouds in the control run (blue lines) and the low-aerosol run (green lines). In Figure 4a, squares represent the precipitation rates observed by rain gauges. The case examined here is a mixed-phase convective cloud system on 17 June 2013 over Guangzhou, China (23.1°N, 113.3°E). The low-aerosol run and the control run include the radiative effects of aerosols, while the other runs do not.

domain-averaged freezing level is 3.5 km, which is consistent with observations. This classification is based on cloud types at each time step and does not consider the transition of warm clouds to cold clouds that occurs over time steps. As seen in comparisons between Figures 4b and 4c, cold clouds produce precipitation with much higher rates than warm clouds. The time- and domain-averaged precipitation rates are 1.16 and 0.90 mm h^{-1} in cold clouds, while the averaged rates are 0.05 and 0.07 mm h^{-1} in warm clouds for the control run and the low-aerosol run, respectively. Implications arising from the times series seen in Figures 4b and 4c are described below.

It is notable that at ~15:00 BJT, aerosol-induced suppression of precipitation turns into aerosol-induced enhancement of precipitation in the control run (as compared to precipitation in the low-aerosol run), which forms the tipping point at ~15:00 BJT (Figure 4a). For the effective identification of mechanisms that control the tipping point, we compare results before 15:00 BJT to those after 15:00 BJT in the following discussions and analyses.

4.2. Precipitation and Updrafts Before 15:00 BJT
4.2.1. Aerosol Radiative Effects Versus No Aerosol Radiative Effects
Stability rises up, and (surface-based and column-integrated) convective available potential energy (CAPE) over noncloudy areas decreases in the simulations with aerosol radiative effects (i.e., the control run and the low-aerosol run) compared to the simulations with no aerosol radiative effects (i.e., the control-no-rad run and the low-aerosol-no-rad run) (Table 1). This is because aerosols absorb solar radiation and heat the atmosphere (Figure 5). In this study, following *Fan et al.* [2013], grid points with total condensed water less (greater) than 10^{-3} g kg^{-1} are categorized as noncloudy (cloudy) grid points or areas. Note that in figures that have height or altitude as the ordinate in this paper, the lowest point on the ordinate corresponds to an altitude of 300 m.

Table 1. The Time- and Domain-Averaged CAPE for the Period Before 15:00 BJT and the Domain-Averaged CAPE at 15:00 BJT Over Noncloudy Areas

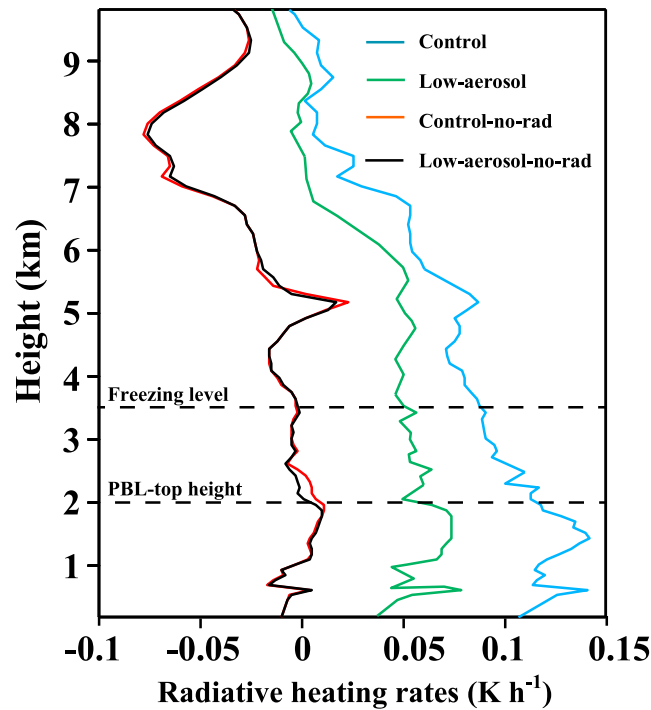|	Between 06:00 BJT and 15:00 BJT				At 15:00 BJT			
	Control	Control-No-Rad	Low-Aerosol	Low-Aerosol-No-Rad	Control	Control-No-Rad	Low-Aerosol	Low-Aerosol-No-Rad
CAPE (J kg^{-1})	1900	2850	2400	2700	3300	2650	3340	2680

Figure 5. Vertical distributions of the time- and domain-averaged radiative heating rates from the ARW model simulations. The control-no-rad run (red line) and low-aerosol-no-rad run (black line) do not include aerosol radiative effects, while the control run (blue line) and the low-aerosol run (green line) include aerosol radiative effects. The low-aerosol run and the low-aerosol-no-rad run have aerosol concentrations that are 10 times lower than those in the control run and the control-no-rad run.

Associated with larger stability in the simulations with aerosol radiative effects than in those with no aerosol radiative effects, as shown in Table 2 and Figure 6a, convection (or updrafts) is suppressed in the control run and the low-aerosol run compared to the control-no-rad run and the low-aerosol-no-rad run before 15:00 BJT. Due to less intense updrafts, there is less condensation, which leads to smaller precipitation rates in the simulations with aerosol radiative effects than in those with no aerosol radiative effects (Table 2 and Figures 4a, 6a, and 7). Greater (smaller) condensation induces more (less) cloud liquid as a source of accretion of cloud liquid by precipitation, which leads to a larger (smaller) amount of precipitation as found by Lee [2011] and Lee et al. [2008a, 2008b].

Before 15:00 BJT, due to the larger updrafts, the transport of cloud-liquid mass to heights above the freezing level by updrafts is greater, leading to larger liquid freezing rates in the simulations with no aerosol radiative effects than in the simulations with aerosol radiative effects (Table 2 and Figure 8a).

Associated with these larger freezing rates, the peak value of the freezing rates is higher in the simulations with no aerosol radiative effects than in those with aerosol radiative effects before 15:00 BJT (Table 2 and Figure 8a).

4.2.2. The Control Run Versus the Low-Aerosol Run

Before 15:00 BJT, the suppression of updrafts is greater in the control run than in the low-aerosol run (Table 2 and Figure 6a). This is because the concentration of absorbing aerosols and thus the heating of the atmosphere are larger in the control run than in the low-aerosol run (Figure 5). Wang et al. [2013] have shown that absorbing aerosols may raise the convection inhibition energy below a cloud but raise CAPE above the convection condensation level (CCL). However, contrary to Wang et al. [2013], in this study, CAPE lowers

Table 2. The Time- and Domain-Averaged Values of Precipitation and Dynamic and Microphysical Variables for Each of the Periods Before and After 15:00 BJT Except for "Updrafts Mass Fluxes in Warm and Cold Clouds" and "Peak Values in the Freezing Rates"[a]

	Between 06:00 BJT and 15:00 BJT				Between 15:00 BJT and 18:00 BJT			
	Control	Control - No-Rad	Low - Aerosol	Low-Aerosol- No-Rad	Control	Control -No-Rad	Low- Aerosol	Low-Aerosol- No-Rad
Precipitation rates (mm h^{-1})	0.61	1.40	0.90	1.24	3.01	1.12	1.20	1.03
Updraft mass fluxes (kg m^{-2} s^{-1})	0.16	0.25	0.19	0.23	0.36	0.18	0.23	0.15
Updraft mass fluxes in warm clouds (kg m^{-2} s^{-1})	0.15	0.28	0.20	0.24	0.18	0.16	0.22	0.15
Updraft mass fluxes in cold clouds (kg m^{-2} s^{-1})	0.72	1.33	0.82	1.11	2.12	1.20	1.51	0.90
Condensation rates (g m^{-3} h^{-1})	0.07	0.13	0.08	0.11	0.12	0.07	0.08	0.06
Freezing rates (10^{-4} g m^{-3} h^{-1})	3.11	18.3	9.32	14.1	21.2	10.0	11.1	8.1
Peak values in the freezing rates (10^{-3} g m^{-3} h^{-1})	1.10	3.50	1.92	2.90	4.01	2.02	2.22	1.91
Autoconversion rates below the freezing level (10^{-5} g m^{-3} h^{-1})	3.35	3.63	8.64	8.97	4.61	3.53	8.58	8.53

[a]The presented values for updrafts mass fluxes in warm (cold) clouds are the averaged updrafts mass fluxes over warm-cloud (cold-cloud) cells, while those for peak values in the freezing rates are the maximum values in the vertical profiles of the averaged freezing rates for each of the periods.
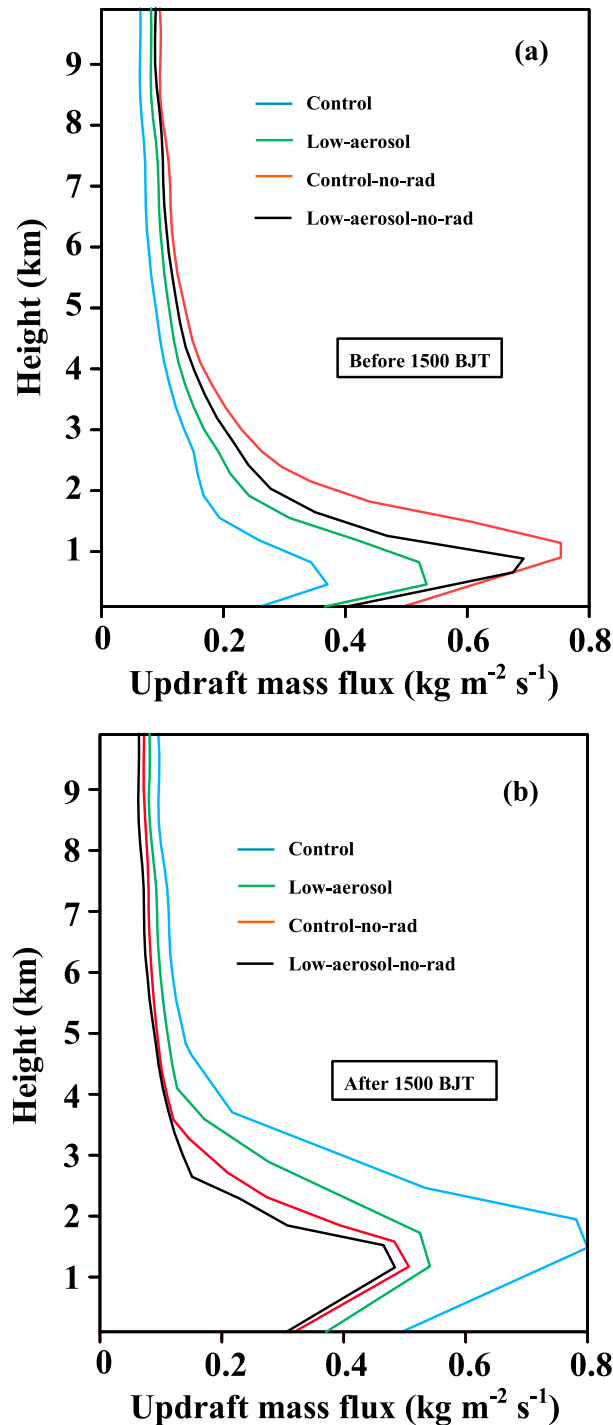
Figure 6. Vertical distributions of the time- and domain-averaged updraft mass fluxes from the ARW model simulations for the period (a) before 15:00 BJT and (b) after 15:00 BJT. Each of the lines depicts the same run as seen in Figures 4a and 5. For the calculation of the averaged updraft mass fluxes, vertical velocities that are greater than $0 \, \text{m s}^{-1}$ are collected and averaged over time and over the domain, after multiplication by their corresponding air densities.

due to absorbing aerosols no matter whether CAPE is placed above the CCL for the period between the beginning of the simulations and 15:00 BJT. This is mainly due to substantial decreases in solar radiation reaching the surface and in surface sensible and latent heat fluxes, leading to a substantial reduction in temperature and humidity near the surface [*Lee et al.*, 2014]. The time- and domain-averaged surface sensible (latent) heat fluxes are 126 (269) and 132 (278) W m^{-2} for the control-no-rad run and the low-aerosol-no-rad run, respectively. The averaged sensible (latent) heat fluxes are 70 (150) and 104 (221) W m^{-2} for the control run and the low-aerosol run, respectively. Here because aerosol concentration declines exponentially above the PBL top around 2 km, differences in aerosol concentration and in aerosol radiative heating between the control run and the low-aerosol run become smaller above ~2 km compared to differences below ~2 km (Figure 5).

A lower liquid freezing rate is seen because less intense updrafts transport a smaller amount of droplets to heights above the freezing level in the control run than in the low-aerosol run before 15:00 BJT (Table 2 and Figures 6a and 8a). As seen in Table 2 and Figure 8a, associated with the lower freezing rate, the peak value of the freezing rate is smaller in the control run than in the low-aerosol run. This smaller liquid freezing rate exists despite aerosol-induced smaller autoconversion and the associated greater cloud-liquid mass as a source of the greater transport and freezing of cloud liquid in the control run as compared to those in the low-aerosol run (Table 2). Hence, aerosol invigoration effects are outweighed by less intense updrafts in the control run than in the low-aerosol run. Here aerosol invigoration effects involve aerosol-induced smaller autoconversion, an associated greater transport of cloud-liquid mass to heights above the level of freezing, and more freezing of cloud liquid in the control run than in
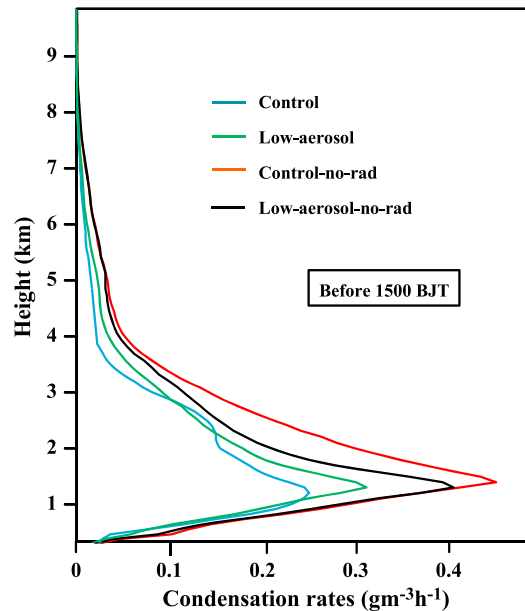
Figure 7. Vertical distributions of the time- and domain-averaged condensation rates from the ARW model simulations for the period before 15:00 BJT. Each of the lines depicts the same run as seen in Figures 4a and 5.

the low-aerosol run. In this situation, the greater stability and associated less intense updrafts result in less condensation and precipitation in the control run than in the low-aerosol run before 15:00 BJT (Tables 1 and 2 and Figures 4a, 6a, and 7).

4.2.3. The Control-No-Rad Run Versus the Low-Aerosol-No-Rad Run

There is an absence of aerosol-induced suppression of updrafts through aerosol radiative effects between the control-no-rad run and the low-aerosol-norad run. With this absence, the reduction in autoconversion and the associated enhancement in cloud-liquid mass below the freezing level in the control-no-rad run (Table 2) lead to the greater transport of cloud liquid to heights above the freezing level. This produces the larger mass of frozen cloud liquid in the control-no-rad run than in the low-aerosol-no-rad run (Figure 8a). This invigorates updrafts more and induces larger updraft mass fluxes and higher precipitation rates in the control-no-rad run than in the low-aerosol-no-rad run during the simulation period (Table 2 and Figures 4a and 6a). As seen in Table 2 and Figure 8a, associated with the larger freezing rates before 15:00 BJT, the peak value of the freezing rate is higher in the control-no-rad run than in the low-aerosol-no-rad run.

4.2.4. Delay in Peak in Precipitation Rate

The enhanced stability in the control run and the low-aerosol run as compared to that in the control-no-rad run and the low-aerosol-no-rad run delays the occurrence of the mature stage of cloud development, which is when peak in precipitation rates occurs. This is regardless of whether the aerosol concentration is high or not as seen in Figure 4a. Peak in precipitation is delayed by 4 h in the control run compared to the control-no-rad run and is delayed by 2 h in the low-aerosol run compared to the low-aerosol-no-rad run. The enhancement in stability in the control run compared to the control-no-rad run is larger than that in the low-aerosol run compared to the low-aerosol-no-rad run (Table 1). This accompanies the greater delay in peak in the precipitation rate in the control run than in the low-aerosol run. This is likely due to the fact that updrafts need longer time to overcome the larger stability to reach their high values at the mature stage. The buildup of the background instability, which determines the occurrence of the mature stage, is controlled by the large-scale forcing and the diurnal cycle of incoming solar radiation. This buildup of the instability and the response of updrafts to it are slowed down more due to aerosol-induced larger increases in stability in the control run than in the low-aerosol run. This is similar to what was reported by *Lee et al.* [2012].

4.3. Precipitation and Updrafts After 15:00 BJT
4.3.1. Aerosol Radiative Effects Versus No Aerosol Radiative Effects

Large-scale moisture and heat convergence and the diurnal cycle of incoming solar radiation favor the occurrence of maximum precipitation rates and associated convection at their mature stage around 13:00 BJT as shown in the control-no-rad run and the low-aerosol-no-rad run in Figure 4a. However, in the control run and the low-aerosol run, updrafts or convection does not grow fully to produce a maximum precipitation rate around 13:00 BJT. This is because aerosol-induced escalation in stability blocks updrafts or convection from growing fully. Associated with this, in the simulations with aerosol radiative effects, the instability from large-scale convergence and the diurnal cycle of incoming solar radiation is not used by updrafts as much as in those runs with no aerosol radiative effects around and before 13:00 BJT. In other words, potential energy is less used or used slower in the simulations with aerosol radiative effects than in those with no aerosol radiative effects.
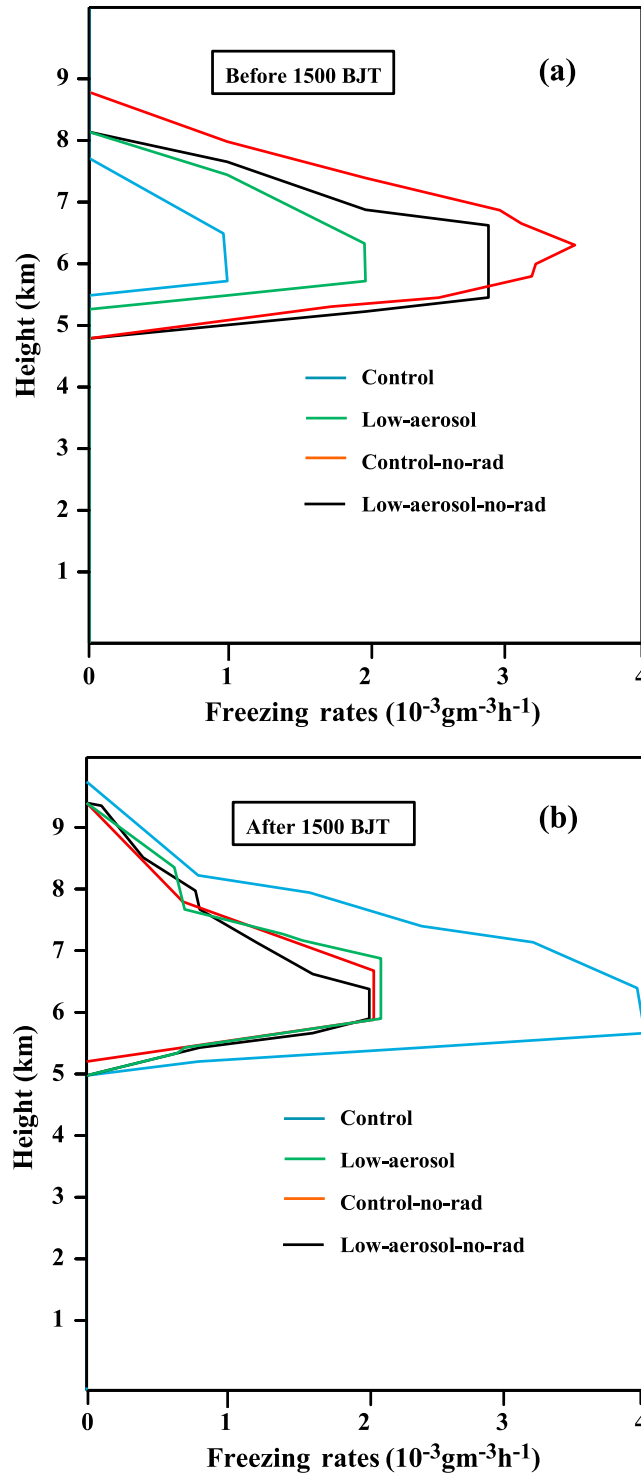
Figure 8. Vertical distributions of the time- and domain-averaged freezing rates from the ARW model simulations for the period (a) before 15:00 BJT and (b) after 15:00 BJT. Each of the lines depicts the same run as seen in Figures 4a and 5. For the calculation of freezing rates, all types of freezing processes (e.g., heterogeneous and homogeneous liquid freezing and riming from collisions between liquid and solid particles) are considered.

The source of potential energy, which is the large-scale convergence and the diurnal cycle of incoming solar radiation, is identical in simulations with and without aerosol radiative effects. The less or slower consumption of potential energy in the simulations with aerosol radiative effects before 13:00 BJT leads to a situation where the potential energy becomes larger in the simulations with aerosol radiative effects than in those with no aerosol radiative effects after 13:00 BJT. The potential energy in the low-aerosol run (control run) becomes larger than that in the simulations with no aerosol radiative effects around 14:00 BJT (15:00 BJT). Hence, the slower consumption of potential energy earlier on enables more available potential energy to be released later on. Here it is notable that CAPE values are similar between the control run and the low-aerosol run around 15:00 BJT (Table 1).

Due to the larger stability, potential energy is used slower in the control run than in the low-aerosol run before 13:00 BJT. Thus, the larger CAPE in the control run compared to that in the simulations with no aerosol radiative effects occurs 1 h later than in the low-aerosol run. Larger CAPE at 15:00 BJT enables stronger updrafts in the simulations with aerosol radiative effects than in those with no aerosol radiative effects after 15:00 BJT (Table 2 and Figure 6b). Averaged updrafts are then obtained over the individual warm-cloud cells and cold-cloud cells. These averaged updrafts over cloud cells are shown in Table 2 and Figure 9. Updrafts tend to become larger in both warm and cold clouds with aerosol radiative effects than with no aerosol radiative effects after 15:00 BJT (Table 2 and Figure 9). Here the number of cloud cells varies by only ~5% for both warm and cold clouds between the periods before and after 15:00 BJT (Table 3). Therefore, it is not the variation in cloud-cell populations but the variation in updrafts in individual cloud cells that is the main cause of the variation in updrafts between the periods before and after 15:00 BJT.
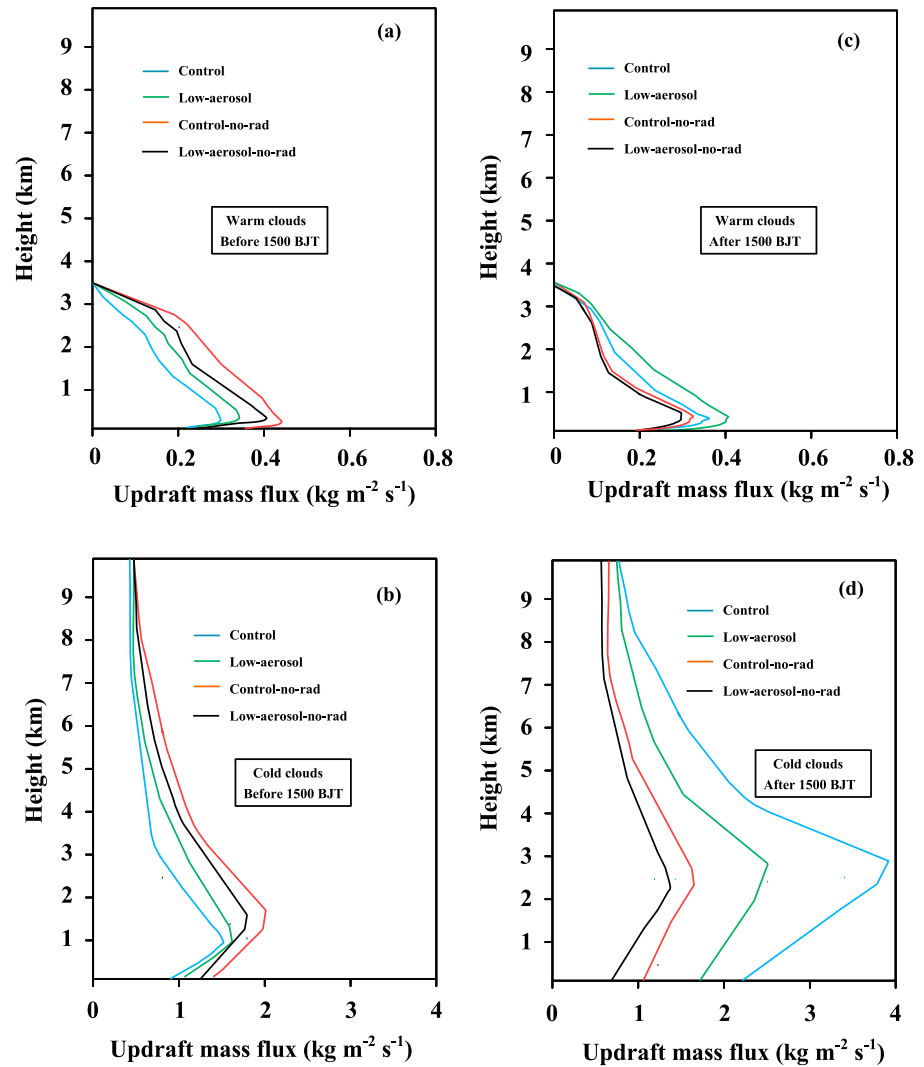
Figure 9. Vertical distributions of the averaged updraft mass fluxes from the ARW model simulations. Vertical distributions of updraft mass fluxes (a and c) averaged over warm clouds and (b and d) averaged over cold clouds. Figures 9a and 9b are averaged over the period before 15:00 BJT, and Figures 9c and 9d are averaged over the period after 15:00 BJT. Each of the lines depicts the same run as seen in Figures 4a and 5. For the calculation of the averaged updraft mass fluxes, vertical velocities that are greater than $0 \, m \, s^{-1}$ are collected and averaged over individual warm clouds or cold clouds, after multiplication by their corresponding air densities.

In contrast to the situation before 15:00 BJT, stronger updrafts induce larger precipitation rates by producing greater condensation in the simulations with aerosol radiative effects than in those with no aerosol radiative effects after 15:00 BJT (Table 2 and Figures 4a, 6, 7, 9, and 10).

4.3.2. The Control Run Versus the Low-Aerosol Run

At 15:00 BJT, the transport of droplets by updrafts to heights above the freezing level is greater in the simulations with aerosol radiative effects than in the simulations with no aerosol radiative effects. This is due to larger CAPE and stronger updrafts that are associated with cold clouds. Around 15:00 BJT, due to similar CAPE, updrafts are similar between the control run and the low-aerosol run. With the similar updrafts around 15:00 BJT, a smaller autoconversion works to induce the greater transport of cloud liquid. This leads to enhanced freezing in the control run compared to that in the low-aerosol run after 15:00 BJT (Table 2 and Figure 8b). This is consistent with the aerosol invigoration effect proposed by *Rosenfeld et al.* [2008]. The domain-averaged autoconversion rates are 3.51×10^{-5} and $8.78 \times 10^{-5} \, g \, m^{-3} \, h^{-1}$ at 15:00 BJT for the control run and the low-aerosol run, respectively.

Table 3. The Cumulative Number of Warm-Cloud and Cold-Cloud Cells for Each of the Periods Before and After 15:00 BJT

	From 06:00 BJT to 15:00 BJT				From 15:00 BJT to 18:00 BJT			
	Control	Control-No-Rad	Low-Aerosol	Low-Aerosol-No-Rad	Control	Control-No-Rad	Low-Aerosol	Low-Aerosol-No-Rad
Warm-cloud cells	6,200	7,100	6,600	6,900	6,400	6,800	6,900	6,700
Cold-cloud cells	9,400	10,200	9,800	9,900	9,700	9,900	10,100	9,600

Larger freezing and related latent heating lead to larger increases in thermal buoyancy and updrafts (compared to thermal buoyancy and updrafts before 15:00 BJT) in the control run than in the low-aerosol run. This leads to stronger updrafts in the control run than in the low-aerosol run after 15:00 BJT (Table 2 and Figures 6a and 6b). The control run shows less intense updrafts than in the low-aerosol run throughout the simulation period in warm clouds, while updrafts in the control run are stronger than those in the low-aerosol run after 15:00 BJT in cold clouds (Figure 9). The different updrafts observed here confirm that the greater transport of droplets to heights above the freezing level and the more freezing of droplets in cold clouds induce the stronger updrafts in the control run than in the low-aerosol run after 15:00 BJT. Associated with the greater freezing and updrafts, a higher fraction of cold clouds is generated for the period between 15:00 BJT and the end of simulations. This in turn leads to a higher faction over the whole simulation period for cold clouds in the control run than in the low-aerosol run as has been reported by *Fan et al.* [2013]. However, as demonstrated by *Fan et al.* [2013], associated with weaker updrafts, we find a lower cloud fraction over the whole simulation period for warm clouds in the control run than in the low-aerosol run. The time- and domain-averaged cloud fraction is 0.36 and 0.31 in the control run and the low-aerosol run, respectively, for cold clouds. The averaged cloud fraction is 0.13 and 0.15 in the control run and the low-aerosol run, respectively, for warm clouds.

After 15:00 BJT, the stronger updrafts trigger much higher condensation rates and, thus, precipitation rates in the control run than in the low-aerosol run [*Lee*, 2011] as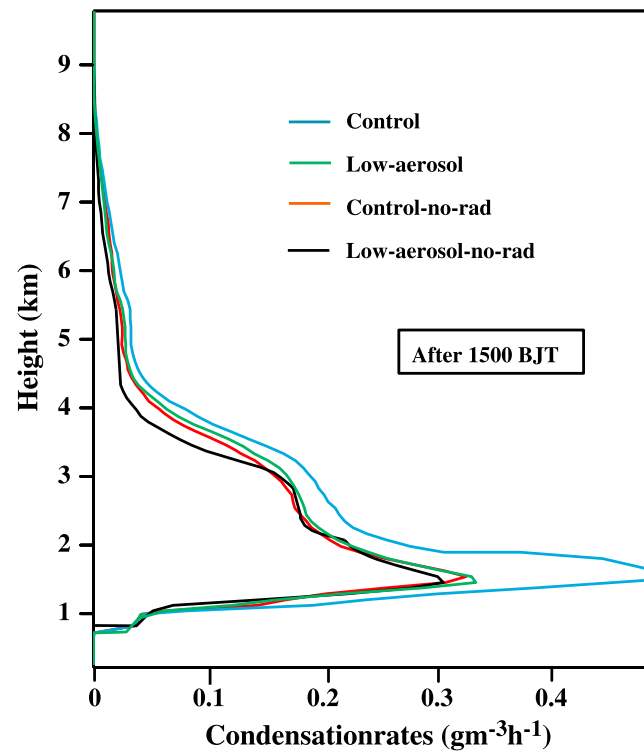 shown in Table 2 and Figures 4a and 10. Note that the higher condensation and freezing rates cause not only the larger hydrometeor loading by enhancing the mass of hydrometeors but also greater latent heating in the control run than in the low-aerosol run. The stronger updrafts demonstrate that the effect of the greater latent heating on updrafts outweighs that of the larger loading in the control run.

In the simulated system, relative humidity in the boundary layer is ~90% which corresponds to a wet environment according to the categorization of environment by *Khain et al.* [2008] and *Lee* [2011]. *Khain et al.* [2008] and *Lee* [2011] have shown that in a dry environment, aerosol-induced increases in condensation may not produce precipitation enhancement. However, in this study, with a wet environment, aerosol-induced higher condensation rates result in higher precipitation rates.

Figure 10. Vertical distributions of the time- and domain-averaged condensation rates from the ARW model simulations for the period after 15:00 BJT. Each of the lines depicts the same run as seen in Figures 4a and 5.

4.3.3. Comparisons of Freezing Rates and Their Peak Values

Freezing rates are higher in the low-aerosol run and the control run than in the simulations with no aerosol

radiative effects for the period between 15:00 BJT and the end of simulations (Table 2 and Figure 8b). Associated with this, the peak values of the freezing rates are also higher in the low-aerosol run and control run than in the simulations with no aerosol radiative effects (Table 2 and Figure 8b). Due to greater instability, CAPE and stronger updrafts at 15:00 BJT, more transport of cloud liquid and freezing occur in the simulations with aerosol radiative effects than in those with no aerosol radiative effects. The larger instability in the simulations with aerosol radiative effects than with no aerosol radiative effects and smaller autoconversion in the control run than in the low-aerosol run work together to produce the highest freezing rate and peak value of the freezing rate in the control run among the four simulations for the period after 15:00 BJT (Table 2 and Figure 8b). This results in the second highest freezing rate and peak value of the freezing rate in the low-aerosol run for the period (Table 2 and Figure 8b).

The smaller transport of cloud liquid, the less freezing of cloud liquid, and the associated lower peak value of the freezing rate occur despite the smaller autoconversion in the control-no-rad run than in the low-aerosol run (Table 2 and Figure 8b). This is due to lower instability and weaker updrafts at 15:00 BJT in the control-no-rad run than in the low-aerosol run. There is the similar instability between the control-no-rad run and the low-aerosol-no-rad run at 15:00 BJT. With this similar instability between the runs, the greater autoconversion in the low-aerosol-no-rad run than in the control-no-rad run leads to the lowest freezing rates and peak value in the low-aerosol-no-rad run among the four simulations for the period after 15:00 BJT (Table 2 and Figure 8b).

4.3.4. Delay in Peak in Precipitation Rates

Just after the time point of CAPE being larger in the low-aerosol run than in the simulations with no aerosol radiative effects, which is 14:00 BJT, the peak in precipitation rate occurs in the low-aerosol run. After ~15:00 BJT, in the control run, aerosol invigoration effects are active as detailed in section 4.3.2. This leads to peak in precipitation rate in the control run that occurs later than in the low-aerosol run by 2 h and 15 min (Figure 4a). This delay in the precipitation rate is similar to the phenomenon found concerning the maximum cloud occurrence under polluted conditions reported by *Fan et al.* [2013] and can be explained by cold clouds (Figure 4b). Also, the greater precipitation rates (related to larger freezing, stronger updrafts, and more condensation) in the control run than in the low-aerosol run that start to show around 15:00 BJT occur in cold clouds but not in warm clouds (Figures 4b and 4c). This indicates that freezing-related invigoration and its competition with aerosol radiative effects are associated with cold clouds. This close association with cold clouds demonstrates that the link between the invigoration effect and its competition with aerosol radiative effects in warm clouds is tenuous due to the absence of freezing in those clouds. This absence of freezing in warm clouds prevents the additional thermal buoyancy that is produced by more freezing of droplets from invigorating updrafts and enhancing precipitation in the control run.

4.4. Simulations With Different Initial Trigger Conditions

In the spirit of ensemble simulations, we repeated the four standard simulations (i.e., the control run, the low-aerosol run, the control-no-rad run, and the low-aerosol-no-rad run) but modified the initial random perturbations of potential temperature. This modification is a way of applying a different initial trigger mechanism to the repeated simulations. The first pair of repeated runs is with initial perturbations lowered by a factor of 2 compared to those in the standard simulations. The second pair is with the initial perturbations increased by a factor of 2 compared to those in the standard simulations. Hence, there are two sets of ensemble simulations and each pair of the repeated runs represents each set of ensemble simulations. Figure 11a presents the same time series as in Figure 4a, along with the time series from simulations with perturbed initial conditions. The basic trends in the repeated runs are similar to those in the standard runs. While this "ensemble" of runs has a limited number of members, results shown in Figure 11a suggest that the analysis presented here is not associated with a particular set of initial trigger conditions.

4.5. Simulations With a Different Domain Size

It is possible that results here can vary with varying domain length, and to test this possibility, the standard simulations are repeated with a larger domain length which is 300 km. These simulations are referred to as the control-300km run, the low-aerosol-300km run, the control-no-rad-300km run, and the low-aerosol-no-rad-300km run. Selecting a domain length of 300 km that is not consistent with the 100 km length of the study area does not allow us to make a reasonable comparison between simulations and observations.
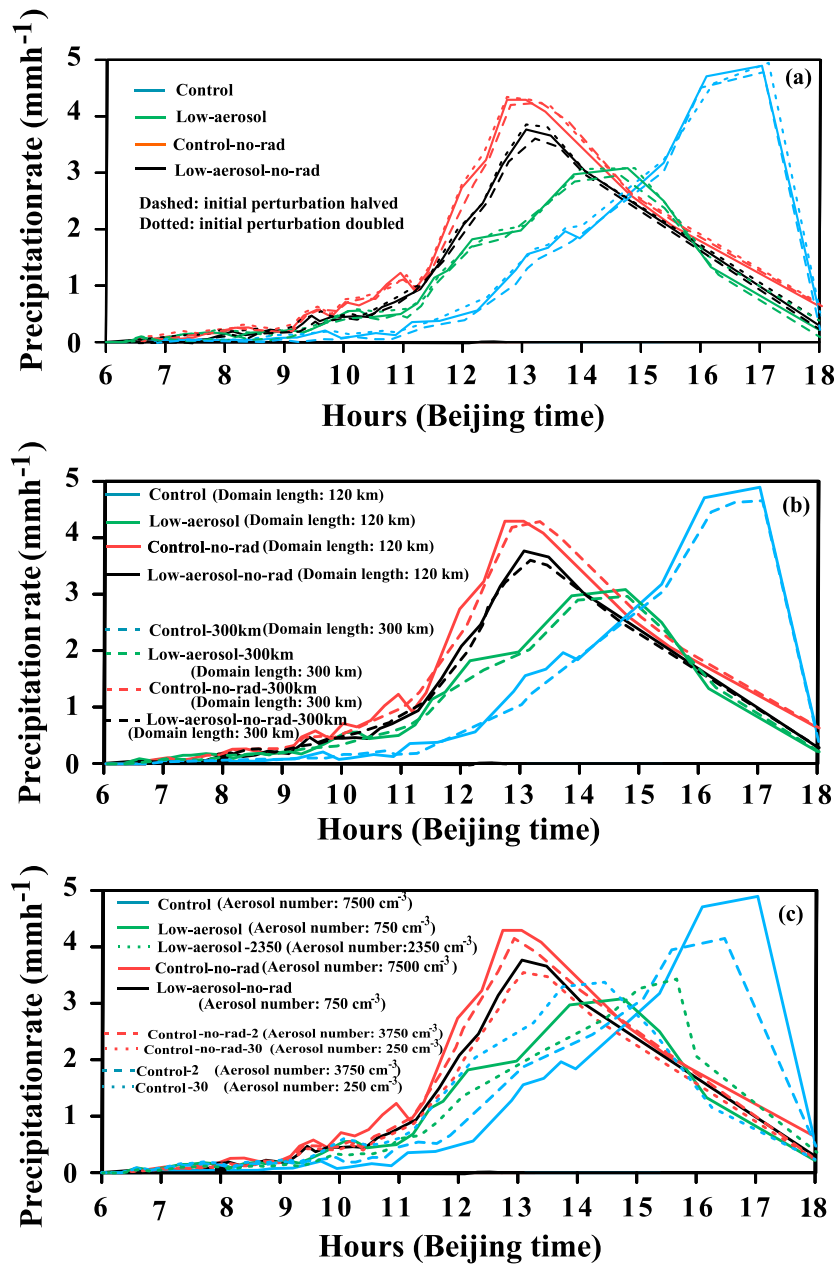
Figure 11. Time series of the domain-averaged precipitation rates from the ARW model simulations. Solid lines are as in Figure 4a. (a) Dashed and dotted lines represent those runs in Figure 4a that are repeated with different initial potential temperature perturbations. The dashed lines show the time series from the repeated runs with the initial perturbations halved, and the dotted lines depict the time series from the repeated runs with the initial perturbations doubled.
(b) Dashed lines represent those runs in Figure 4a that are repeated with the domain length that is elongated from 120 km to 300 km. (c) Dashed blue and red lines represent the control run and the control-no-rad run that are repeated with aerosol concentration reduced by a factor of 2, while dotted blue and red lines represent the control run and the control-no-rad run that are repeated with aerosol concentration reduced by a factor of 30 as compared to that in the control run and the control-no-rad run, respectively. The dotted green line represents the low-aerosol run that is repeated with the averaged aerosol concentration of 2350 cm^{-3} over the PBL.

Despite this, these repeated runs can help toward evaluating the robustness of the results to the model setup, e.g., domain size.

As shown in Figure 11b, these repeated runs show results that are not qualitatively different from those with the standard runs. This demonstrates that results here are quite robust to the choice of the domain size. This

is consistent with the findings reported by *Phillips and Donner* [2007]. *Phillips and Donner* [2007] compared results obtained by averaging an ensemble of 85 small (~100 km) domains to those from a single large (~5000 km) domain and found that their statistical behaviors are similar. They attributed this to the fact that the size of individual convection, which is around 5–30 km, is much smaller than the size of the domain and thus the impact of the size of the domain on individual convection is not significant.

4.6. Simulations With Different Aerosol Perturbations

To test the robustness of results here to different aerosol concentrations for the low-aerosol simulations, we repeated the control run and the control-no-rad run by reducing aerosol concentrations by factors of 2 and 30, respectively. The repeated simulations with the reduced aerosol concentration by a factor of 2 are referred to as the control-2 run and the control-no-rad-2 run, respectively. Those simulations with the reduced aerosol concentration by a factor of 30 are referred to as the control-30 run and the control-no-rad-30 run, respectively. The averaged aerosol concentration over the PBL in the control-2 run and the control-no-rad-2 run is $3750 \, \text{cm}^{-3}$ that is higher than $750 \, \text{cm}^{-3}$ in the low-aerosol run and the low-aerosol-no-rad run. In the control-30 run and the control-no-rad-30 run, the PBL-averaged aerosol concentration is $250 \, \text{cm}^{-3}$ that is lower than $750 \, \text{cm}^{-3}$ in the low-aerosol run and the low-aerosol-no-rad run.

Similar to the low-aerosol-no-rad run, the control-no-rad-30 run and the control-no-rad-2 run show smaller precipitation rates than the control-no-rad run (Figure 11c). However, due to lower (higher) aerosol concentrations and associated less (more) freezing and invigoration, precipitation rates are lower (higher) in the control-no-rad-30 run (the control-no-rad-2 run) than in the low-aerosol-no-rad run (Figure 11c). This demonstrates that the qualitative nature of the results here is not sensitive to the level of aerosol concentrations for low-aerosol simulations, when it comes to simulations with no aerosol radiative effects.

Similar to what is seen in the low-aerosol run and the low-aerosol-no-rad run, due to aerosol radiative effects, precipitation is suppressed in the control-30 run and the control-2 run compared to that in the low-aerosol-no-rad run before 15:00 BJT (Figure 11c). However, the suppression is lesser (greater) due to the lower (higher) aerosol concentration that absorbs solar radiation in the control-30 run (control-2 run) than in the low-aerosol run.

After 15:00 BJT, the control-30 run shows results that are qualitatively similar to the low-aerosol run with respect to the control run (Figure 11c). Of interest is that in the control-2 run, there are substantial increases in precipitation and the occurrence of the precipitation peak which are similar to those in the control run and are not present in the low-aerosol run and the control-30 run after 15:00 BJT (Figure 11c). This is due to larger aerosol concentration and the associated greater invigoration of convection in the control-2 run than in the low-aerosol run and the control-30 run. However, due to a smaller aerosol concentration and the associated less invigoration, the precipitation rates and their peak are lower in the control-2 run than in the control run (Figure 11c). This suggests that there is a critical level of aerosol concentration above which peaks in precipitation rates can be generated.

To find the critical level, we repeated the low-aerosol run by gradually increasing aerosol concentrations. In the repeated runs, the averaged aerosol concentration over the PBL increases in the increments of $100 \, \text{cm}^{-3}$ from an initial value of $750 \, \text{cm}^{-3}$ to a value for which the first occurrence of a precipitation peak after 1500 BJT is seen. When the averaged concentration reaches $2350 \, \text{cm}^{-3}$, the precipitation peak starts to appear in one of the runs, i.e., the low-aerosol-2350 run in Figure 11c. Thus, $2350 \, \text{cm}^{-3}$ is determined to be the estimated critical level of aerosol concentration.

4.7. Simulations With Aerosol Layers at Different Altitudes

As described in section 3, in the standard runs, the main aerosol layer is located in the PBL below ~2 km. Remember that in the main layer, aerosol concentration remains constant; however, beyond the main layer, aerosol concentration decreases exponentially. It has been shown that convective clouds in the tropics entrain a significant amount of environmental air above the PBL [*McGee and van den Heever*, 2014]. Hence, it is possible that aerosol particles are transported to levels above the PBL in our study area, which can lead to heating in the atmosphere and cooling near the surface that are quantitatively different from those shown in the standard runs. Motivated by this possibility, the standard runs are repeated by shifting the main aerosol layer upward in altitude. Since the simulated cloud system is rooted in low-level clouds below an altitude of
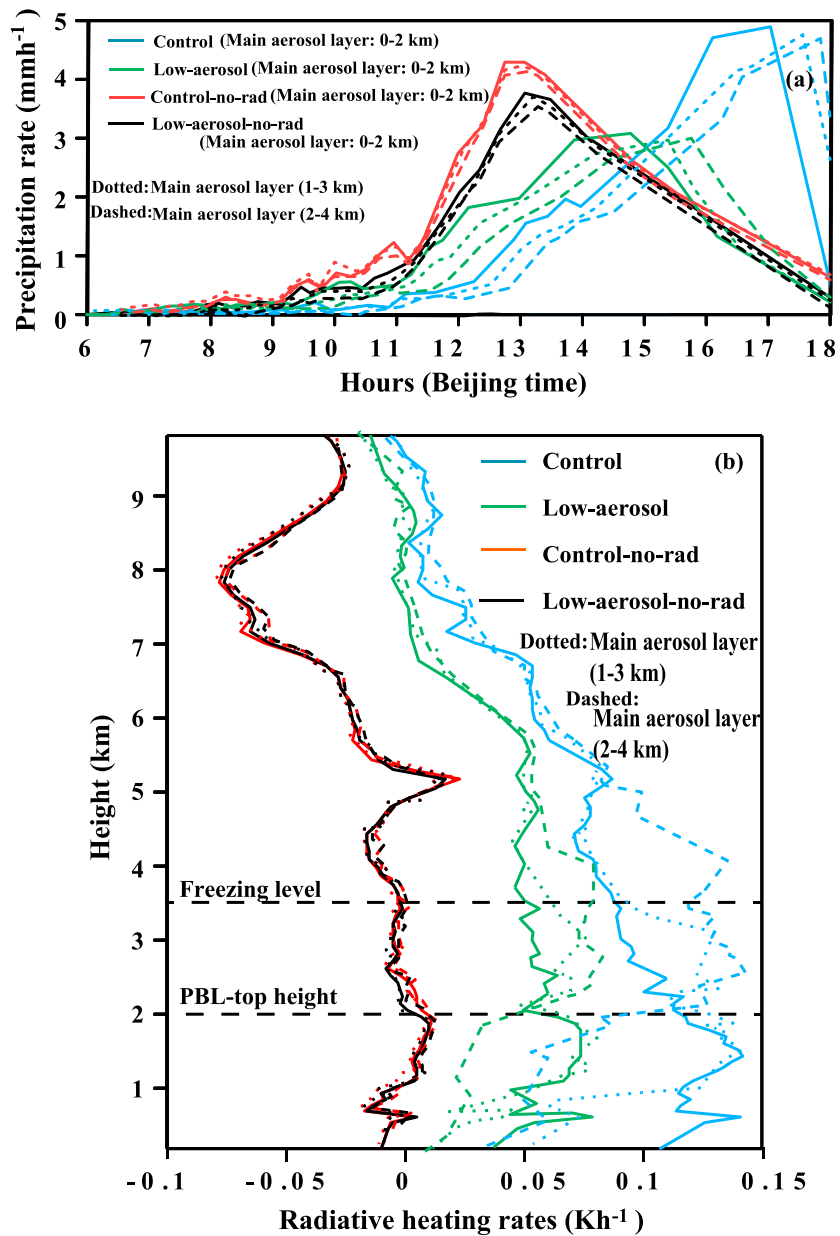
Figure 12. (a) Time series of the domain-averaged precipitation rates from the ARW model simulations and (b) vertical distributions of the time- and domain-averaged radiative heating rates from the simulations. Solid lines are as in Figures 4a and 5. Dashed and dotted lines represent those runs in Figures 4a and 5 that are repeated with different altitudes of the main aerosol layer. The dotted lines show results from the repeated runs with the layer between 1 and 3 km, and the dashed lines depict those results from the repeated runs with the layer between 2 and 4 km.

~4 km, these clouds essentially drive the development of the cloud system. Hence, we focus on clouds below 4 km in determining the location of the layer. For the first set of the repeated simulations, represented by dotted lines in Figure 12a, the layer is located at altitudes between 1 and 3 km that correspond to those around the middle part of clouds below 4 km. For the second set of the repeated simulations, represented by dashed lines in Figure 12a, the layer is located at altitudes between 2 and 4 km that correspond to those around the upper part of clouds below 4 km. In the first and second sets of the repeated control run and control-no-rad run, the averaged aerosol concentration in the layer is $7500 \, cm^{-3}$. In the first and second sets of the repeated low-aerosol run and low-aerosol-no-rad run, the averaged aerosol concentration in the layer is $750 \, cm^{-3}$. Aerosol concentrations decrease exponentially below and above the layer in question.

Associated with this, larger differences in aerosol radiative heating are located in and around the layer between 1 and 3 km compared to those in other layers for the first set of the repeated runs (Figure 12b). The larger differences are located in and around the layer between 2 and 4 km for the second set of the repeated runs (Figure 12b).

Figure 12a shows that the qualitative nature of the results here does not depend on the altitude of the main aerosol layer. However, as shown by *Wang et al.* [2013] and *Lee et al.* [2014], as the altitudes of the layer rise, so do aerosol-induced increases in stability over the layer below 4 km. Hence, compared to the repeated runs with no aerosol radiative effects, precipitation in the repeated runs with aerosol radiative effects is suppressed and this suppression enhances before 15:00 BJT compared to the situation in the standard runs. Also, peak in precipitation rates occurs later in the repeated control run (as compared to the control run) and in the repeated low-aerosol run (as compared to the low-aerosol run).

4.8. Simulations With No Effects of Freezing on Temperature

To better understand the roles played by aerosol-induced changes in the freezing in the results here, the standard runs are repeated with the effects of freezing on latent heating and temperature turned off. However, freezing affects the mass of solid-phase particles in these repeated runs. In these repeated runs, the effects of other processes (e.g., melting), which affect latent heating and cooling, on temperature are present. These repeated runs are referred to as the control-no-freez run, the low-aerosol-no-freez run, the control-no-rad-freez run, and the low-aerosol-no-rad-freez run. There are lower precipitation rates in the control-no-rad-freez run than in the low-aerosol-no-rad-freez run (Figure 13a). This is due to the absence of aerosol-induced increases in freezing-related latent heating and the associated invigoration of convection over the simulation period. This demonstrates that aerosol-induced rising freezing rates, the impacts on latent heating and associated invigoration, play an important role in the higher precipitation rates in the control-no-rad run than in the low-aerosol-no-rad run. The invigoration here involves enhancement of the hydrometeor mass and loading. However, the effect of latent heating on invigoration dominates over that of the loading, resulting in stronger updrafts and higher precipitation rates in the control-no-rad run.

Due to aerosol radiative effects and associated larger stability, before 15:00 BJT, precipitation rates are lower in the control-no-freez run and the low-aerosol-no-freez run (with the effect of aerosol on radiation) than in the control-no-rad-freez run and the low-aerosol-no-rad-freez run (with no effect of aerosol on radiation) (Figure 13a). Due to the larger concentration of aerosol and greater stability, precipitation rates are lower in the control-no-freez run than in the low-aerosol-no-freez run before 15:00 BJT (Figure 13a).

After 15:00 BJT, precipitation becomes larger in the control-no-freez run and the low-aerosol-no-freez run than in the control-no-rad-freez run and the low-aerosol-no-rad-freez run due to more available convective energy. This is also simulated in the standard runs and explained in sections 4.2 and 4.3. However, because there is no effect of greater freezing on latent heating, after 15:00 BJT, there are negligible differences in precipitation between the control-no-freez run and the low-aerosol-no-freez run. This demonstrates that it is aerosol-induced enhancement in freezing-related latent heating that induces the higher precipitation rates and the occurrence of peak in precipitation rates after 15:00 BJT in the control run compared to the rates and the absence of peak in the low-aerosol run.

Figures 13b and 13c show the vertical profiles of condensation rates before and after 15:00 BJT. Due to the absence of increases in freezing-related latent heating and associated invigoration in the control-no-rad-freez run, condensation is less in the control-no-rad-freez run than in the low-aerosol-no-rad-freez run over the simulation period. This leads to the lower precipitation rates in the control-no-rad-freez run than in the low-aerosol-no-rad-freez run, which is in contrast to the higher condensation rates, leading to more precipitation in the control-no-rad run than in the low-aerosol-no-rad run (Figures 4a, 7, 10, and 13).

After 15:00 BJT, there are no increases in freezing-related latent heating and no associated invigoration in the control-no-freez run. Due to this, condensation is slightly less in the control-no-freez run than in the low-aerosol-no-freez run, in contrast to the situation between the control run and the low-aerosol run (Figure 13c). This indicates that the changes in condensation (or diffusional growth of droplets) are a by-product of the response of freezing-related latent heating to aerosol but not the primary factor that drives the differences in precipitation or associated invigoration between the simulations as discussed by *Lee* [2011].
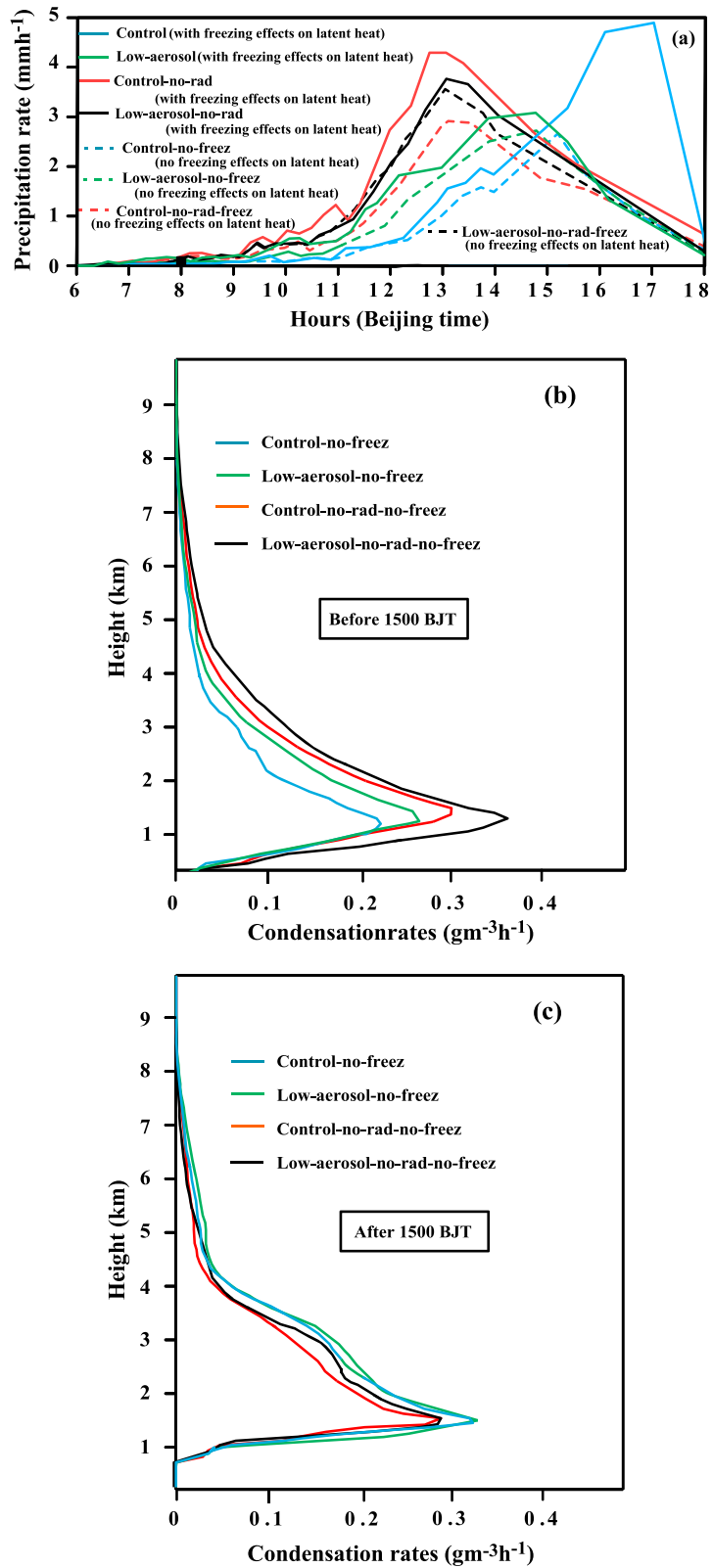
Figure 13. (a) Time series of the domain-averaged precipitation rates from the ARW model simulations and vertical distributions of the time- and domain-averaged condensation rates from the simulations for the period (b) before 15:00 BJT and (c) after 15:00 BJT. Solid lines in Figure 13a are as in Figure 4a. Dashed lines in Figure 13a and solid lines in Figures 13b and 13c represent those runs in Figure 4a that are repeated with the effects of freezing on latent heating turned off.

As shown by *Lee* [2011], the variation in latent heating by freezing with varying aerosol concentration is at least 1 order of magnitude smaller than the variation by condensation (Table 2 and Figures 7, 8, and 10). The time- and domain-averaged variation in condensation (freezing) rate is 3.00×10^{-2} (3.60×10^{-4}) $g\,m^{-3}\,h^{-1}$ between the control-no-rad run and the low-aerosol-no-rad run over the simulation period. After 15:00 BJT, the time- and domain-averaged variation in condensation (freezing) rate is 4.00×10^{-2} (1.01×10^{-3}) $g\,m^{-3}\,h^{-1}$ between the control run and low-aerosol run. However, as shown by *Lee* [2011], despite the much smaller variation in freezing, aerosol-induced changes in freezing trigger those in condensation. Aerosol-induced enhancement in freezing-related latent heating first strengthens updrafts, and this in turn induces more deposition above the freezing level. Increases in deposition are roughly ~1 order of magnitude greater than those in freezing and thus further strengthen updrafts above the freezing level. To satisfy mass conservation, these stronger updrafts above the freezing level induce more intense cloud-bottom convergence, which accompanies stronger updrafts below the freezing level where most of condensation occurs and thus greater condensation. Greater condensation and stronger updrafts establish feedbacks between them, which result in a much larger aerosol-induced variation in condensation than that in freezing.

4.9. Discussion of the Sensitivity of Results to Microphysics Parameterization

Fan et al. [2012] have pointed out that the use of a fixed CDNC, a saturation adjustment, and constant collection efficiencies in double-moment schemes is the main cause of discrepancies in aerosol effects on clouds and precipitation between bin schemes and double-moment schemes. However, the double-moment scheme adopted in this study uses predicted CDNCs, predicted supersaturation levels, and varying collection efficiencies with varying hydrometeor sizes. So we believe that the results here are less affected by the shortcomings of double-moment schemes discussed by *Fan et al.* [2012]. This belief is further supported by *Khain et al.* [2015] who concluded that the use of bin schemes or the type of the bulk scheme used in this study is desirable for reasonable simulations of aerosol-cloud interactions. However, it should be noted that the bulk scheme used here assumes a gamma size distribution with fixed breadth for hydrometeors. As pointed out by *Khain et al.* [2015], this assumption can lead to errors in the representation of microphysics and its interactions with aerosol. Further studies are required to better understand the impacts of the assumption on clouds and their interactions with aerosol. However, the repetition of standard simulations done in this study using different types of size distribution (i.e., exponential and lognormal distributions) shows that results here do not depend on the specific choice of size distribution.

In addition to the representation of CDNC, saturation, and collection processes, the representation of hail can be another cause of discrepancies in aerosol effects on clouds and precipitation between bin schemes and double-moment schemes [*Loftus and Cotton*, 2014]. Note that the representation of hail (e.g., hail size) in this study is more simplified than that in the bin- and three-moment schemes discussed by *Loftus and Cotton* [2014]. However, comparisons of precipitation properties (e.g., precipitation rates and amount) between observations and the control run show a good agreement in this study (Figure 4a). Hence, we think that precipitation processes including those related to hail are simulated reasonably well despite the simplified representation of hail in this study. Moreover, we repeated the control run by excluding hail from hydrometeors and found that the precipitation properties from this repeated simulation agree well with observations. This indicates that for the cloud system adopted in this study, hail or its representation in the model does not play an important role in the reasonable simulation of precipitation.

5. Summary and Conclusions

Severe convective weather systems that produce thunderstorms and heavy rainfall generally exhibit diurnal cycles over land. In Part 1 of our companion studies, *Guo et al.* [2016] have found a systematic difference in the peak of the occurrence of such events under polluted and clean conditions, postulating that aerosols have a discernible impact on the diurnal cycle of severe weather events. To test the hypothesis and to gain further insight into the causes of the observed different diurnal cycle patterns between clean and polluted conditions reported by *Guo et al.* [2016], numerical simulations are performed using a full-fledged CSRM that accounts for aerosol microphysical and radiative effects.

Results show that between 06:00 BJT and 15:00 BJT, the aerosol radiative effect leads to suppressed convection and lowered precipitation rates in the control run (corresponding to polluted conditions) compared to

those in the low-aerosol run (corresponding to clean conditions). This is despite the reduction in autoconversion and associated enhancement in cloud-liquid mass in the control run. This enhancement in cloud-liquid mass is supposed to increase cloud-liquid freezing, which would invigorate convection and increase precipitation. However, the higher concentration of aerosol that acts as a radiation absorber induces greater stability and generates less intense updrafts in the control run than in the low-aerosol run. This outweighs the invigoration effects or aerosol microphysical effects, leading to suppressed convection and precipitation in the control run.

Due to the large stability induced by aerosol radiative effects, potential energy is used slower, which leads to the extended buildup of potential energy before 15:00 BJT. After 15:00 BJT, this generates instability and potential energy that are large enough to help the aerosol invigoration effect to produce higher precipitation rates in the control run than in the low-aerosol run. Due to the larger stability before 15:00 BJT and the greater amount of time required for updrafts to overcome this stability, peak in precipitation rate occurs 2 h and 15 min later in the control run than in the low-aerosol run. This corroborates the delay of precipitation observed under polluted conditions in the Pearl River Delta region of southern China as described in Part 1.

Results from the control run and the low-aerosol run are robust to the altitudes of the main aerosol layer. Also, the occurrence of a peak in precipitation in the control run depends on the level of aerosol concentration. When the level is below a critical value, the peak does not appear. This demonstrates that a minimum level of aerosol concentration is needed for a peak to appear. The estimated minimum level for the case simulated in this study is 2350 cm^{-3}. Once aerosol concentration reaches this minimum level, a large enough reduction in autoconversion and a large enough increase in cloud-liquid mass induce the invigoration of convection that in turn is strong enough to generate a peak.

This study demonstrates that aerosol effects on clouds alter the diurnal variation in clouds and precipitation and identifies associated preliminary mechanisms. We believe that these mechanisms are a valuable stepping stone toward a better understanding of the diurnal variation in the context of aerosol-cloud-radiation interactions, considering that the level of understanding of aerosol effects on the diurnal variation has been low thus far. These mechanisms demonstrate that to get a better picture of aerosol effects on the diurnal variation, we have to delve into interactions or competition between aerosol radiative effects and aerosol microphysical effects.

References

Ackerman, A. S., O. B. Toon, D. E. Stevens, A. J. Heymsfield, V. Ramanathan, and E. J. Welton (2000), Reduction of tropical cloudiness by soot, *Science*, *288*, 1042–1047.

Chen, F., and J. Dudhia (2001), Coupling an advanced land surface-hydrology model with the Penn State-NCAR MM5 modeling system. Part I: Model implementation and sensitivity, *Mon. Weather Rev.*, *129*(4), 569–585.

Davidi, A., I. Koren, and L. Remer (2009), Direct measurements of the effect of biomass burning over the Amazon on the atmospheric temperature profile, *Atmos. Chem. Phys.*, *9*, 8211–8221.

Donner, L. J., C. J. Seman, and R. S. Hemler (1999), Three-dimensional cloud-system modeling of GATE convection, *J. Atmos. Sci.*, *56*(12), 1885–1912.

Fan, J., L. R. Leung, Z. Li, H. Morrison, H. Chen, Y. Zhou, Y. Qian, and Y. Wang (2012), Aerosol impacts on clouds and precipitation in eastern China: Results from bin and bulk microphysics, *J. Geophys. Res.*, *117*, D00K36, doi:10.1029/2011JD016537.

Fan, J., L. R. Leung, D. Rosenfeld, Q. Chen, Z. Li, J. Zhang, and H. Yan (2013), Microphysical effects determine macrophysical response for aerosol impact on deep convective clouds, *Proc. Natl. Acad. Sci. U.S.A.*, *110*, doi:10.1073/pnas.1316830110.

Feingold, G., and S. M. Kreidenweis (2002), Cloud processing of aerosol as modeled by a large eddy simulation with coupled microphysics and aqueous chemistry, *J. Geophys. Res.*, *107*(D23), 4687, doi:10.1029/2002JD002054.

Feingold, G., H. Jiang, and J. Y. Harrington (2005), On smoke suppression of clouds in Amazonia, *Geophys. Res. Lett.*, *32*, L02804, doi:10.1029/2004GL021369.

Fouquart, Y., and B. Bonnel (1980), Computation of solar heating of the Earth's atmosphere: A new parameterization, *Beitr. Phys. Atmos.*, *53*, 35–62.

Fridlind, A. M., et al. (2012), A comparison of TWP-ICE observational data with cloud-resolving model results, *J. Geophys. Res.*, *117*, D05204, doi:10.1029/2011JD016595.

Fridlind, A., A. Ackerman, J. Petch, P. Field, A. Hill, G. McFarquhar, S. Xie, and M. Zhang (2010), ARM/GCSS/SPARC TWP-ICE CRM intercomparison study. [Available at http://pubs.giss.nasa.gov/abs/fr08100v.html.]

Grabowski, W. W. (2006), Indirect impact of atmospheric aerosols in idealized simulations of convective–radiative quasi equilibrium, *J. Clim.*, *19*, 4664–4682.

Guo, J. P., X. Y. Zhang, Y. R. Wu, H. Z. Che, B. La, and X. Li (2011), Spatio-temporal variation trends of satellite-based aerosol optical depth in China during 1980–2008, *Atmos. Environ.*, *45*(37), 6802–6811, doi:10.1016/j.atmosenv.2011.03.068.

Guo, J., M. Deng, J. Fan, Z. Li, Q. Chen, P. Zhai, Z. Dai, and X. Li (2014), Precipitation and air pollution at mountain and plain stations in northern China: Insights gained from observations and modeling, *J. Geophys. Res. Atmos.*, *119*, 4793–4807, doi:10.1002/2013JD021161.

Guo, J., M. Deng, S. S. Lee, F. Wang, Z. Li, P. Zhai, H. Liu, W. Lv, W. Yao, and X. Li (2016), Delaying precipitation and lightning by air pollution over the Pearl River Delta: 1. Observational analyses, *J. Geophy. Res. Atmos.*, *121*, 6472–6488, doi:10.1002/2015JD023257.

Hansen, J. E., M. Sato, and R. Ruedy (1997), Radiative forcing and climate response, *J. Geophys. Res.*, *102*, 6381–6864, doi:10.1029/96JD03436.

Hill, A. A., and S. Dobbie (2008), The impact of aerosols on non-precipitating marine stratocumulus. II: The semi-direct effect, *Q. J. R. Meteorol. Soc.*, *134*, 1155–1165.

Jacobson, M. Z. (2006), Effects of externally-through-internally-mixed soot inclusions within clouds and precipitation on global climate, *J. Phys. Chem. A*, *110*, 6860–6873.

Jacobson, M. Z. (2012), Investigating cloud absorption effects: Global absorption properties of black carbon, tar balls, and soil dust in clouds and aerosols, *J. Geophys. Res.*, *117*, D06205, doi:10.1029/2011JD017218.

Kessler, E. (1969), On the distribution and continuity of water substance on atmospheric circulation, *Meteorol. Monogr.*, *10*(32), 84.

Khain, A., and B. Lynn (2009), Simulation of a supercell storm in clean and dirty atmosphere using weather research and forecast model with spectral bin microphysics, *J. Geophys. Res.*, *114*, D19209, doi:10.1029/2009JD011827.

Khain, A., D. Rosenfeld, and A. Pokrovsky (2005), Aerosol impact on the dynamics and microphysics of deep convective clouds, *Q. J. R. Meteorol. Soc.*, *131*, 2639–2663.

Khain, A., N. BenMoshe, and A. Pokrovsky (2008), Factors determining the impact of aerosols on surface precipitation from clouds: Attempt of classification, *J. Atmos. Sci.*, *65*, 1721–1748.

Khain, A. P., et al. (2015), Representation of microphysical processes in cloud resolving models: Spectral (bin) microphysics versus bulk parameterization, *Rev. Geophys.*, *53*, 247–322, doi:10.1002/2014RG000468.

Koch, D., and A. D. Del Genio (2010), Black carbon semi-direct effects on cloud cover: Review and synthesis, *Atmos. Chem. Phys.*, *10*, 7685–7696, doi:10.5194/acp-10-7685-2010.

Koren, I., Y. J. Kaufman, L. A. Remer, and J. V. Martins (2004), Measurement of the effect of Amazon smoke on inhibition of cloud formation, *Science*, *303*(5662), 1342–1345, doi:10.1126/science.1089424.

Koren, I., J. V. Martins, L. A. Remer, and H. Afargan (2008), Smoke invigoration versus inhibition of clouds over the Amazon, *Science*, *321*(5891), 946–949, doi:10.1126/science.1159185.

Lee, S. S. (2011), Dependence of aerosol-precipitation interactions on humidity in a multiple-cloud system, *Atmos. Chem. Phys.*, *11*(5), 2179–2196.

Lee, S. S. (2012), Effect of aerosol on circulations and precipitation in deep convective clouds, *J. Atmos. Sci.*, *69*, 1957–1974.

Lee, S. S., and G. Feingold (2010), Precipitating cloud-system response to aerosol perturbations, *Geophys. Res. Lett.*, *37*, L23806, doi:10.1029/2010GL045596.

Lee, S. S., L. J. Donner, V. T. J. Phillips, and Y. Ming (2008a), The dependence of aerosol effects on clouds and precipitation on cloud-system organization, shear and stability, *J. Geophys. Res.*, *113*, doi:10.1029/2007JD00922.

Lee, S. S., L. J. Donner, V. T. J. Phillips, and Y. Ming (2008b), Examination of aerosol effects on precipitation in deep convective clouds during the 1997 ARM summer experiment, *Q. J. R. Meteorol. Soc.*, *134*(634), 1201–1220, doi:10.1002/qj.287.

Lee, S. S., L. J. Donner, and J. E. Penner (2010), Thunderstorm and stratocumulus: How does their contrasting morphology affect their interactions with aerosols? *Atmos. Chem. Phys.*, *10*, 6819–6837, doi:10.5194/acp-10-6819-2010.

Lee, S. S., G. Feingold, and P. Y. Chuang (2012), Effect of aerosol on cloud-environment interactions in trade cumulus, *J. Atmos. Sci.*, *69*(12), 3607–3632, doi:10.1175/JAS-D-12-026.1.

Lee, S. S., G. Feingold, I. Koren, H. Yu, T. Yamaguchi, and A. McComiskey (2014), Effect of gradients in biomass burning aerosol on circulations and clouds, *J. Geophys. Res. Atmos.*, *119*, 9948–9964, doi:10.1002/2014JD021819.

Li, Z. (1998), Influence of absorbing aerosols on the inference of solar surface radiation budget and cloud absorption, *J. Clim.*, *11*, 5–17.

Li, Z., K.-H. Lee, J. Xin, Y. Wang, and W.-M. Hao (2010), First observation-based estimates of aerosol radiative forcing at the top, bottom and inside of the atmosphere, *J. Geophys. Res.*, *115*, D00K18, doi:10.1029/2009JD013306.

Li, Z., F. Niu, J. Fan, Y. Liu, D. Rosenfeld, and Y. Ding (2011), Long-term impacts of aerosols on the vertical development of clouds and precipitation, *Nat. Geosci.*, *4*, 888–894.

Loftus, A. M., and W. R. Cotton (2014), A triple-moment hail bulk microphysics scheme. Part II: Verification and comparison with two-moment bulk microphysics, *Atmos. Res.*, *150*, 97–128.

McGee, C. J., and S. C. van den Heever (2014), Latent heating and mixing due to entrainment in tropical deep convection, *J. Atmos. Sci.*, *71*, 816–832, doi:10.1175/JAS-D-13-0140.1.

Mlawer, E. J., S. J. Taubman, P. D. Brown, M. J. Iacono, and S. A. Clough (1997), RRTM, a validated correlated-k model for the longwave, *J. Geophys. Res.*, *102*, 16,663–16,682, doi:10.1029/97JD00237.

Morrison, H., and W. W. Grabowski (2011), Cloud-system resolving model simulations of aerosol indirect effects on tropical deep convection and its thermodynamic environment, *Atmos. Chem. Phys.*, *11*, 10,503–10,523.

Pan, H.-L., and L. Mahrt (1987), Interaction between soil hydrology and boundary-layer development, *Bound.-Layer Meteorol.*, *38*, 185–202.

Peng, J. F., et al. (2014), Submicron aerosols at thirteen diversified sites in China: Size distribution, new particle formation and corresponding contribution to cloud condensation nuclei production, *Atmos. Chem. Phys.*, *14*(18), 10,249–10,265, doi:10.5194/acp-14-10249-2014.

Phillips, V. T. J., and L. J. Donner (2007), Cloud microphysics, radiation, and vertical velocities in two- and three-dimensional simulations of deep convection, *Q. J. R. Meteorol. Soc.*, *133*, 3011–3033.

Rosenfeld, D., U. Lohmann, G. B. Raga, C. D. O'Dowd, M. Kulmala, S. Fuzzi, A. Reissell, and M. O. Andreae (2008), Flood or drought: How do aerosols affect precipitation? *Science*, *321*(5894), 1309–1313.

Saleeby, S. M., and W. R. Cotton (2004), A large-droplet mode and prognostic number concentration of cloud droplets in the Colorado State University Regional Atmospheric Modeling System (RAMS). Part I: Module descriptions and supercell test simulations, *J. Appl. Meteorol.*, *43*, 182–195, doi:10.1175/JAM2312.1.

Segal, M., J. Weaver, and J. F. W. Purdom (1989), Some effects of the Yellowstone fire smoke plume on northeast Colorado at the end of summer 1988, *Mon. Weather Rev.*, *117*, 2278–2283.

Seifert, A., and K. D. Beheng (2006), A two-moment cloud microphysics parameterization for mixed-phase clouds. Part 2: Maritime vs. continental deep convective storms, *Meteorol. Atmos. Phys.*, *92*, 67–82.

Skamarock, W. C., J. B. Klemp, J. Dudhia, D. O. Gill, D. M. Barker, W. Wang, and J. G. Powers (2008), A description of the Advanced Research WRF, version 3. NCAR Tech. Note NCAR/TN-4751STR, 113 pp.

Storer, R. L., S. C. van den Heever, and G. L. Stephens (2010), Modeling aerosol impacts on convection under differing storm environments, *J. Atmos. Sci.*, *67*, 3904–3915.

Tao, W. K., J. P. Chen, Z. Li, C. Wang, and C. D. Zhang (2012), Impact of aerosols on convective clouds and precipitation, *Rev. Geophys.*, *50*, RG2001, doi:10.1029/2011RG000369.

Tao, W.-K. (2007), Cloud resolving modeling, *J. Meteorol. Soc. Jpn.*, *85*, 305–330.

Tao, W.-K., X. Li, A. Khain, T. Matsui, S. Lang, and J. Simpson (2007), Role of atmospheric aerosol concentration on deep convective precipitation: Cloud-resolving model simulations, *J. Geophys. Res.*, *112*, D24S18, doi:10.1029/2007JD008728.

Ten Hoeve, J. E., M. Z. Jacobson, and L. A. Remer (2012), Comparing results from a physical model with satellite and in situ observations to determine whether biomass burning aerosols over the Amazon brighten or burn off clouds, *J. Geophys. Res.*, *117*, D08203, doi:10.1029/2011JD016856.

van den Heever, S. C., G. G. Carrio, W. R. Cotton, P. J. DeMott, and A. J. Prenni (2006), Impacts of nucleating aerosol on Florida storms. Part I: Mesoscale simulations, *J. Atmos. Sci.*, *63*, 1752–1775.

van den Heever, S. C., and W. R. Cotton (2007), Urban aerosol impacts on downwind convective storms, *J. Appl. Meteorol. Climatol.*, *46*, 828–850.

van den Heever, S. C., G. L. Stephens, and N. B. Wood (2011), Aerosol indirect effects on tropical convection characteristics under conditions of radiative–convective equilibrium, *J. Atmos. Sci.*, *68*, 699–718.

van Zanten, M. C., et al. (2011), Controls on precipitation and cloudiness in simulations of trade-wind cumulus as observed during RICO, *J. Adv. Model. Earth Syst.*, *3*, M06001, doi:10.1029/2011MS000056.

Varble, A. C., A. Fridlind, E. Zipser, A. Ackerman, J.-P. Chaboureau, J. Fan, A. Hill, S. A. McFarlane, J.-P. Pinty, and B. Shipway (2011), Evaluation of cloud-resolving model intercomparison simulations using TWP-ICE observations: Precipitation and cloud structure, *J. Geophys. Res.*, *116*, D12206, doi:10.1029/2010JD015180.

Wang, Y., A. Khalizov, M. Levy, and R. Zhang (2013), New directions: Light absorbing aerosols and their atmospheric impacts, *Atmos. Environ.*, *81*, 713–715, doi:10.1016/j.atmosenv.2013.09.034.

Xu, K.-M., et al. (2002), An intercomparison of cloud-resolving models with the atmospheric radiation measurement summer 1997 intensive observation period data, *Q. J. R. Meteorol. Soc.*, *128*(580), 593–624, doi:10.1256/003590002321042117.

Zhang, X. Y., Y. Q. Wang, T. Niu, X. C. Zhang, S. L. Gong, Y. M. Zhang, and J. Y. Sun (2012), Atmospheric aerosol compositions in China: Spatial/temporal variability, chemical signature, regional haze distribution and comparisons with global aerosols, *Atmos. Chem. Phys.*, *12*(2), 779–799, doi:10.5194/acp-12-779-2012.